Picosecond laser beam nanostructuring of GDC thin films: exchange surface enhancement by LIPSS

Wael Karim, Agnès Petit, Hervé Rabat, Malek Tabbal, Anne-Lise Thomann, Nadjib Semmar

Picosecond laser beam nanostructuring of GDC thin films: exchange surface enhancement by LIPSS

Wael Karim[1], Agnès Petit[1], Hervé Rabat[1], Malek Tabbal[2], Anne-Lise Thomann[1] and Nadjib Semmar[1*]

1. GREMI-UMR 7344-CNRS-University of Orleans, 14 Rue d'Issoudun, BP6744, 45067 Orléans Cedex, France

2. Department of Physics, American University of Beirut, Beirut, Lebanon 1107 2020.

Corresponding authors:** ***Nadjib.semmar@univ-orleans.fr

Abstract

In ceramic electrochemical cells, gadolinium-doped ceria (GDC) thin film is deposited between the electrolyte (yttria-stabilized zirconia, YSZ) and the upper electrode in order to improve the aging resistance. Increasing the interface surface area is expected to be beneficial to the cell performance. This work deals with the investigation of LIPSS (Laser induced periodic surface structures) formation on the surface of a 600 nm GDC thin films , grown by magnetron sputtering on screen-printed YSZ. A picosecond Nd: YAG laser operating at its third harmonic (λ=355 nm, 40 ps, 10Hz) was used for structuring the surface of the GDC/YSZ layer after deposition, thanks to static and scanning irradiation modes. The different structures formed on the films' surface following laser irradiation, mainly quasi-periodic LIPSS, were investigated by Scanning Electron Microscopy (SEM) and Atomic Force Microscopy (AFM). Parallel and perpendicular LIPSS were simultaneously formed with periods varying from 220 to 300 nm, function of the beam fluence ranging from 30 to 160 mJ/cm^2, and within a spot size of ~500 µm in the static mode. The coexistence of both orientations disapear at higher number of shots (N > 20) to form only parallel structures. As increasing the number of shots up to N> 50, a progressive ablation of the film occurs to start again the process of YSZ substrate nano-structuring. The formation of parallel LIPSS is mainly attriduted to the thermochemical process that occurs on the GDC/YSZ film in the center of the irradiated zone corresponding to the higher local fluence. The same LIPSS orientations were perfomed also in the scaning mode by varying the laser fluence and the scanning stage parameters. For the last mode, the effect of laser irradiation on the elemental composition of the films was investigated by Energy Dispersive X-Ray spectroscopy (EDX) and Rutherford Back-Scattering (RBS) to check the film chemical stability under the process of soft ablation by accumulation effect. Finally, the

surface area enhancement by LIPSS formation was estimated thanks to Atomic Force Microscopy (AFM) and using a geometrical enhancement coefficient that returns a 'theoretical' maximum values of 57% and 78 % for 1D (regular LIPSS) and 2D periodic structures respectively

Keywords: Picosecond laser beam, oxide thin film, GDC magnetron sputtered film, multi-pulse irradiation, LIPSS.

Highlights

- LIPSS formation have been achieved on gadolinium doped ceria (GDC) thin films under static and scanning beam modes.
- Laser texturing is performed using a pico-second Nd:YAG laser with a beam spot diameter close to 500 µm.
- Experimental conditions for the obtention of parallel and perpendicular LIPSS and the occurrence of film ablation were determined.
- Results are explained through the existence of soft ablation by incubation effects and thermochemical process at higher local fluence.
- The surface enhancement due to laser texturing is estimated over 30% using AFM and a geometrical model.

Graphical abstract

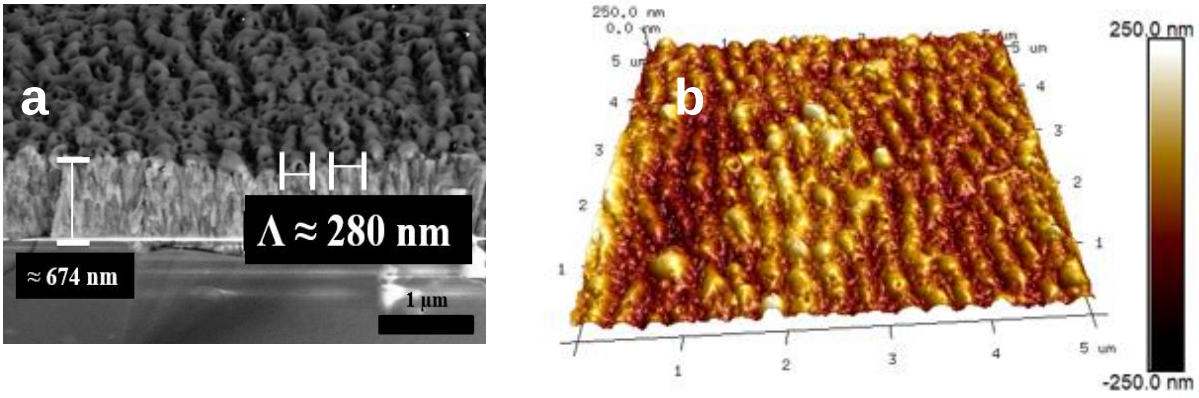

Introduction

The interaction between ultrashort laser beam pulses with solid state materials can result in formation of surface micro/nanostructures that are commonly referred to as Laser Induced Periodic Surface Structures (LIPSS). The size, shape and distribution of these structures show a complex dependence on the experimental conditions (such as laser energy, wavelength, repetition rate, scanning speed) as well as the type of material irradiated (metals, semiconductor, dielectric, ceramic or polymer) [1-7]. An understanding of LIPSS formation and a good control of their characteristics is crucial since their presence significantly modifies the surface properties of the material which could thus be "tuned" for a specific application. LIPSS formation has indeed been shown to improve the mechanical and wetting properties of surfaces in addition to several other applications in a wide array of technological fields [8-13]. Building on the potential of laser texturing of the surface of bulk material, LIPSS formation on thin films form has recently generated great interest both from the fundamental and technological aspects [14-17]. Compared to the case of bulk materials, the physico-chemical processes occurring during the laser irradiation of a thin film are markedly altered, typically with the observation of a lowering of the material's ablation threshold, the occurrence of cavitation as well as thermomechanical fragmentation as examples [18-21]. From a technological viewpoint, LIPSS formation on thin films could provide an attractive one-step approach to materials' micro/nano-structuring for functional coatings and advanced devices.

This work specifically deals with the investigation of LIPSS formation on the surface of gadolinium-doped ceria (GDC) thin films, grown by magnetron sputtering on screen-printed yttria-stabilized zirconia (YSZ). The GDC and YSZ are complex oxides that are employed in solid ceramic cells technology [22-24] namely due to their high ionic conductivity. A thin layer of GDC sandwiched between the electrolyte and the upper electrode ($La_{1-x}Sr_xCo_{1-y}Fe_yO_{3-\delta}$) can act as a diffusion barrier and has been found to improve the lifetime of cells dedicated to the production of hydrogen by high temperature electrolysis. With the aim to improve the efficiency of the cell, one interesting approach would be to increase the surface area where the electrochemical reactions take place, namely the actual area of the interface between the electrolyte (YSZ) and the upper electrode. A picosecond Nd: YAG laser operating at third harmonic (λ=355 nm) was used for structuring the surface of the GDC layer after deposition, both in static and scanning modes. The different structures formed on the films' surface following laser irradiation were investigated by Scanning Electron Microscopy (SEM) and Atomic Force Microscopy (AFM). A mapping of the different surface morphologies as a function of irradiation conditions was thus achieved for the static mode. The effect of laser

irradiation on the elemental composition of the films was also investigated by Energy Dispersive X-Ray spectroscopy (EDX) and Rutherford Back-Scattering (RBS). Surface area enhancement by LIPSS formation was finally discussed using a simple model based on the morphological arrangement of the induced nanostructures.

Experimental

Gadolinium-doped ceria (GDC) thin films, with thicknesses of around 600 nm were deposited by direct current magnetron sputtering of 4-inch diameter metallic $Ce_{1-x}Gd_x$ target (x=0.2) on screen printed Yttrium-Stabilized Zirconium (YSZ) substrates (having thicknesses $\geq$ 1 µm). All deposition runs were performed at a pressure of 1 Pa with 20 sccm of Ar as a sputtering gas and 2 sccm of O_2 as a reactive gas, while the substrates were not heated during the growth. The as-deposited films were subsequently annealed in air at 500 ^oC, a process that resulted in highly crystalline and stoichiometric layers ($Ce_{1-x}Gd_xO_2$). More details about growth conditions and films properties were presented elsewhere by Mickan et al. [25].

The laser irradiation experiments were achieved using a picosecond Nd: YAG laser operating at its third harmonic (λ =355 nm) with a pulse duration of 40 ps and 10 Hz repetition rate. The corresponding irradiation process is shown on Fig.1. The energy/pulse is modulated using a set of optical filters (UGC from Thorlabs), and the Gaussian beam of the laser is then focused on the surface of the sample using a quartz lens having a focal distance of 75 mm. For the present study, the laser fluence of the incident beam (F) could be varied from 30 to 125 mJ/cm^2.

Samples were irradiated in static mode (by accumulation of successive single-spots) and in scanning mode (large-area irradiation achieved by S-scanning) in air under atmospheric conditions. In the case of static mode, the total number of shots (N) irradiating the same area of the sample is accurately controlled via an automated opto-mechanical shutter. Under scanning mode conditions, the sample is mounted on a motorized X, Y computer controlled scanning stage. In order to irradiate the whole surface of the films, an S-shaped scanning pattern is achieved via a LabVIEW interface. The sample is moved along the x-axis at a speed V_x and displaced by a distance ΔY (perpendicular to the x-axis) at the end of the motion. The values of V_x used in the work could be varied from 50 µm/s up to 5 mm/s.

The surface morphology of the thin films before and after laser irradiation were observed using a Carl Zeiss SMT SUPRA 40 Field Emission Gun SEM, and their chemical

composition determined using the EDX. LIPSS amplitude and periodicity were determined through surface imaging using a Bruker AFM. Finally, RBS analysis was performed using α particles of 2 MeV extracted from a Pelletron accelerator in the CEMHTI laboratory (CNRS-Orléans, France).

Results

Irradiation under static mode

Figure 2 shows a typical SEM image of the surface of a GDC film irradiated under static mode with 10 laser pulses at a fluence of 125 mJ/cm^2 and a large spot size close to 500 µm. Careful observation allows us to delimit several different regions on the image corresponding to the insets within the figure. First, the non-irradiated surface of the GDC films exhibits the grain boundaries of the polycrystalline YSZ layer (micron-sized grains) decorated by the GDC film [25]. The laser impact region reasonably approximated to be circular, with a diameter $W_0 \approx 500$ µm, can be distinguished within which, two nearly circular concentric regions were imaged by SEM at higher resolution (see insets). The two different regions correspond to the formation of unexpected periodic patterns having different orientations with respect to the beam polarization. Quasi-regular LIPSS with orientation perpendicular to the laser beam (see bottom inset of the figure) are visible on the boarder of the irradiated zone. These LIPSS are formed at lower energy density (keeping in mind the beam Gaussian distribution) and are found to have a spatial period $\Lambda \sim 265 \pm 10$ nm, lower than the laser wavelength (λ=355 nm), and denoted as LSFL$\perp$. Indeed, in the center of the laser spot, that corresponds to the highest local fluence, unexpected LIPSS oriented parallel to the polarization of the laser beam with a spatial period of about 245 ± 10 nm are also observed and denoted as LSFL$_{//}$, as indicated in the bottom inset of the figure 2. The formation of two LIPSS patterns with different spatial periods and different directions was already observed in the case of HSFL and LSFL formation within the same spot zone [26] [27], on several metal and dielectric materials as well as on polymer thin films [28-30], but rarely on complex oxide substrate with very close spatial periods. Using similar picosecond laser at the fourth harmonic (266 nm), T.T.D. Huynh et al. [16] found LSFL with a period of 260 nm on the surface of a Cu thin film. After increasing the number of shots to a very high values, the HSFL and dots LIPSS were formed. Considering another metallic film but under scanning mode, Dostovalov et al. [31] have found on the Cr surface, irradiated with a femtosecond laser (τ = 232 fs; λ = 1026 nm; f =

200 kHz), LSFL-like structures (Λ_{LSFL} = 696, 704, 816, and 858 nm) for scanning speed V = 1, 10, 50 and 100 μm/s, respectively. In both works, the obtained LSFL are in the range 0,6 to 0,9λ, parallel to the laser beam polarization, which are very similar to our unexpected case of $LSFL_{//}$ structures. On the contrary, A. Talbi et al. [17] have managed to texture a thin layer of the dielectric (titanium oxide $TiO_{1.2}$) and obtained perpendicular LSFL structures perpendicular to the beam polarization with period of 800 nm, using a femtosecond laser of wavelength 1030 nm with pulse duration of 500 fs. As earlier reported in several theories debating on LIPSS mechanism [12][32-33], formation of LIPSS parallel or perpendicular to the laser beam polarization is mainly related to the nature of the material surface (electronic properties, optical, thermal…) and the laser beam features (polarization, intensity, repetition rate…). Dostovalov et al. [34] studied the mechanism of LIPSS formation in Cr thin film material subject to oxidation process. The oxidation level (depending on the film thickness) during the irradiation was identified to induce a significant change on the optical properties as a consequence of the physico-chemical nature of the oxide film, and thus on the LIPSS orientation, parallel or perpendicular to the beam polarization. This particular 'thermochemical' conditions leading to oxidation process during the irradiation of thin metal films were also investigated by Oktem et al [35] that proposed a new paradigm through the positive feedback approach for highly regular LIPSS. In such cases, the formed nanostructures are identified as thermochemical LIPSS (TLIPSS). To support this assumption (TLIPSS formation) for the $LSLF_{//}$ formed on GDC/YSZ in the center of the irradiated zone further chemical investigation are needed for example by using XPS analysis (not shown in the present work) for an accurate estimation of the oxygen contribution. On other side, it has been found in literature that above 700°C, annealed GDC can lose part of its oxygen content. This leads to an increase of the non-stoichiometric coefficient δ ($Ce_{0.8}Gd_{0.2}O_{2-\delta}$), which can induce a lattice expansion, commonly referred to "chemical expansion". This would originate from the growth of the cation radii during the reduction reactions taking place inside the CGO layers [36][37]. Thus, the Ce^{4+} ions incorporated in CGO transform respectively into Ce^{3+} ions, which can locally generate a mixed ionic electronic conductivity (MIEC) [38]. As previously mentioned, due to the Gaussian beam distribution, the local fluence is highest at the center of the laser spot, so that the temperature can locally exceed the value (considering also the reaction time over this temperature threshold) at which GDC acquires MIEC properties. This induces like a *transient* 'metallic' behavior followed by intense oxidation that probably induces the formation of $LSFL_{//}$.

Further inspection of the LIPSS formation at different laser fluences have led to finding a dependence of the LIPSS spatial period on laser fluence as shown in Figure 3 for both the types of LIPSS, the LSFL$_{//}$ and the LSFL$_{\perp}$. Indeed, the figure shows that the spatial periods for each type get closer to each other as laser fluence is increased from 60 mJ to 125 mJ/cm^2, with the increasing (decreasing) from 220 (300) to 245 (265) nm, respectively. The values of the spatial periods thus range from 0.6λ to 0.85λ, and those are known to depend on the refractive index n of the irradiated material. This also tends to confirm the correlation between the oxidation stage, the chemical expansion and thus the optical properties changes. Thanks to the results reported in Dostovalov et al. [34], the diminution of LSFL$_{\perp}$ period versus fluence is related to the 'soft' ablation process and the film thickness reduction, while the slight increase of LSFL$_{//}$ period is attributed to the chemical expansion phenomenon followed by more intense re-oxidation. Notice that in such complex situation, intermediate like-2D structures are localized in the transition zone between the center and rim of the irradiated zone as previously shown on fig. 2.

To investigate the (F, N) domain of LIPSS formation and their singular orientation, the fluence and the number of shots are regularly increased up to the full ablation of the GDC film. Figure 4 shows SEM images on the surface of the GDC/YSZ samples irradiated at laser fluences between 40 and 125 mJ/cm^2, and numbers of shots ranging from 10 to 70. Different surface morphologies are then observed depending on laser fluence and number of laser pulses. Indeed, at the lowest fluence, namely 40 mJ/cm^2, LSFL$_{\perp}$ are observed at N=10 and N=40, Fig 4.a and 4.b, respectively. In the latter case whoever, the LIPSS do not look as regularly formed. Increasing the number of pulses to 70 leads to the loss of the LIPSS patterns by ablation and re-deposition of the GDC films (Fig. 4.c). Upon increase of laser fluence for values of 105 and 125 mJ/cm^2, both parallel and perpendicular LIPSS are still formed, as shown in Fig.4.d and Fig.4.g where the reported SEM images were taken at different places of the irradiated area (separated by the red line in the figure). As shown before, the LSFL$_{\perp}$ were found near the borders of the laser spot, and the LSFL$_{//}$ appear in the center. Static irradiation with 30 pulses at 105 mJ/cm^2 leads to the loss of the LIPSS pattern (Fig.4.e) and this becomes more pronounced after 50 pulses (Fig.4.f) where the crystalline grain boundaries of the underlying YSZ become exposed. It is noteworthy that the loss of LIPSS pattern takes place at a smaller number of pulses with increasing laser fluence, i.e. at 30 laser pulses at 105 mJ/cm^2 instead of 70 for laser fluence of 40 mJ/cm^2. At even higher fluence, 125 mJ/cm^2, and after 30 and 50

laser pulses, the GDC film appears to be completely ablated and is accompanied by patterning of the YSZ into square shapes.

Further insight on the SEM results presented in Fig.4 is obtained through a determination of the chemical composition of the surfaces after laser irradiation. To that end, the representative EDX signals for films irradiated at different laser fluences and number of laser pulses are reported in Fig.5, along with that of the untreated film. Insets are included in the figure corresponding to SEM images shown in Fig. 4. The EDX signals of the untreated sample (Fig.5.a) and that of a film irradiated with 10 pulses at 40 mJ/cm^2 (Fig.5.b) exhibiting LIPSS, indicate a similar chemical composition, namely the composition of GDC films, with no signal emanating from the underlying YSZ substrate. This confirms that the LIPSS patterns formed retain, within the accuracy limit of EDX, the same chemical composition as the starting material. With the loss of LIPSS formation for N = 70 at the same laser fluence (Fig.5.c), the EDX signals from the Ce and Gd are still detected but in addition to a broad peak corresponding to Y and Zr (the overlapping signals from these two elements is due to their close atomic masses, 89 and 91 u). This confirms the onset of ablation suggested from the SEM image for these irradiation conditions (Fig.4.c). With further increase of laser fluence (150 mJ/cm^2) and a number of pulses of 40, the EDX signal of Y/Zr peak is dominant as the signal from Ce and Gd atoms become much weaker. This confirms that the square-shaped pattern seen in the inset of Fig.5.d can be attributed to laser surface structuring of the YSZ substrate (though some traces of the GDC films may remain). These patterns are quite similar to those obtained at 125 mJ/cm^2 for N = 30 and 50, Fig.4.h and i, and evidence the almost complete ablation of the GDC film.

Based on the parametric study presented above, a mapping of the laser induced surface modification of the GDC films grown on YSZ is suggested in Fig.6, as laser fluence and number of laser pulses are varied from 30 to 150 mJ/cm^2 and 1 to 70, respectively. The SEM and EDX observations allow us to delimit five distinguishable domains whose formation is dependent on the local energy dose. To resume:

LIPSS formation is not possible for F < 40 mJ/cm^2 (presented in Gray). At higher fluence values (85 to 125 mJ/cm^2), LSFL$_{//}$ and LSFL$_{\perp}$ (in Red) could be generated but with N<20

- LSFL$_{\perp}$ only (in Blue)
- Ablation of GDC before texturing of YSZ substrate (in Green)
- Full ablation of GDC and Structuring of YSZ in squares shapes (in Purple)

Each phenomenon exists in a given area of the plot that means over a given range of fluence and number of laser pulses. For instance, talking about the ablation process, it occurs at higher laser pulse number when the fluence is decreased. This is the indication that the ablation threshold is related to a parameter proportional to F*N (total deposited energy dose), which is the sign of an incubation phenomenon. The same behavior is observed for the formation of both kinds of LSFL. In Figure 7, we present a schematic that depicts the various energy dose thresholds for the formation of perpendicular and parallel LIPSS as well as the threshold for GDC full ablation that also corresponds to the starting point of YSZ structuring.

Irradiation under scanning mode

To estimate the enhancement of the exchange surface on GDC film we did achieve laser irradiation on a wide surface are (minimum 4 X 4 mm^2) by moving the sample holder on the X, Y directions as indicated on fig1. Thanks to an automated scanner system (Scanner Newport-Conex CC with accessible speed ranging form 0,01 to 5 mm/s in the X, Y directions, with a translation path ΔY = 100 µm).

The starting point of our scanning strategy is based on the (F, N) mapping plot (fig.6) to reproduce on a large scale the LIPSS with the two main findings of the static mode:

for condition (F=125 mJ/cm^2, N<20) corresponding to LSFL$_{//}$ and LSFL$_{\perp}$ domain, and (F = 85 mJ/cm^2, 20 < N < 30) related to only LSFL$_{\perp}$ domain. Results for both operating conditions are plotted on figure 8 when the N becomes N_{eff} calculated from a standard formula that links the repetition rate ***f***, the sport size ***d*** to the scanner speed $\boldsymbol{V_X}$ and the transverse path $\boldsymbol{\Delta Y}$ (i.e., $\boldsymbol{N_{eff} = (d*f)/Vx*(d/\Delta Y)}$). As shown on the corresponding SEM images, if the second condition reproduce similar regular structures as in the static mode, the first one (F=125 mJ/cm^2, $\boldsymbol{N_{eff}}$ = 25) shows more complex patterns due to the superposition of parallel and perpendicular LSFL induces by the overlap of the successive irradiations. Also, we did the same EDX analyses as for the static mode with similar conclusions for the CGO film. However some redeposit is observed for the higher fluence (F=125) suggesting the examination of the limit parameters to achieve the ablation (full) of the film.

For this purpose, we have investigated laser irradiation of the GDC films for F = 40, 85, 125 and 150 mJ/cm^2 under two scanning (low) speeds 0.2 and 0.4 mm/s ($\boldsymbol{N_{eff}}$ = 125, 65,5 respectively). SEM images of such laser irradiated surfaces are shown in Fig. 9. For F = 40 mJ/cm^2, no LIPSS are detected for a scanning speed of 0.4 mm/s (Fig.9.a1) but some regular rippling indicating the onset of LIPSS formation is observed at 0.2 mm/s, (Fig.9.a2). Increasing the value of laser fluence to 85 mJ/cm^2, LIPSS are formed even at the higher scanning speed of 0.4 mm/sec (Fig.9.b1), and appears somewhat similar to those obtained at 0.2 mm/sec (Fig.9.b2). This implies that the energy threshold to obtain LIPSS is reached even at the higher speed. Further increase of laser fluence up to 125 mJ/cm^2 still results in well-ordered LIPSS at V = 0.4 mm/s (Fig.9.c1) but at lower scanning speed (0.2 mm/s) ablation of the thin layer of GDC takes place (Fig.9.c2). Finally, for the highest laser fluence used in this work, namely 150 mJ/cm^2, GDC film ablation is observed at V = 0.4 mm/s (Fig.9.d1) and becomes nearly complete at V = 0.2 mm/s (Fig.9.d2). Indeed, at such speed and laser fluence, the grain boundaries of the YSZ substrate become exposed and the substrate itself becomes regularly patterned into square shaped structures as observed for the highest laser fluence and number of pulses in the static irradiation case (Fig. 6.j). As indicated previously, during this ablation process we have only reproduced the LSFL$_{\perp}$ before the full removal of the GDC thin film

Figure 10 shows two SEM images of the cross section of the GDC layer. The first one is the untreated layer and the other one a layer textured by laser scanning at a fluence of 85 mJ/cm2 and a velocity V = 0.4 mm/s. First of all it is clearly visible that the GDC film in depth mirosctructure greatly changes. The well aligned columns of about 100 nm width are not present any more, and have been remplaced by less regular patterns. It can be also noticed that the thickness of the layer has decreased by a value of about 100 nm that confirms the partiel ablation occuring for this condtions.

In addition, RBS measurements, illustrated in Figure 11, were performed on these two samples to confirm the thickness reduction after laser structuring. From simulation of the spectra, it can be deduced that there was a decrease in the Ce and Gd atoms/cm^2 after laser treatment, while the proportions of YSZ and O can be kept unchanged. And finally, the shape of the spectra at the interface between GDC and YSZ layers inidcates that the roughness of the layer becomes more important, which is in good agreement with the SEM images of figure 10.

Estimation of the surface area increase by LIPSS

The surface modification due to the formation of nanostructures could be evaluated through some simple geometrical considerations. We propose to estimate the surface enhancement due to the LIPSS fabrication using the geometrical model detailed in Appendix section. From the set of equations (6* and 7*), the maximum theoretical enhancement coefficient (Σ) cannot exceed 57% in the case of regular 1D LIPSS and 78% in the case of 2D LIPSS (nanodots, nanobumps…). This maximum is only achieved in the case of contiguous LIPSS, that means $2r \approx \Lambda$, where r is here the specific radius size of the nanostructure (assumed uniform), and Λ the spatial period. However, the major case of LIPSS configurations corresponds to the case $2r/\Lambda < 1$, and as reported in Table 1, the estimation of the enhancement coefficient Σ returns values in the range 10 to 40%. From sizes obtained on *Fig. 12 (more resolved cross section and tilted SEM image)*, we performed the same estimation of the Σ coefficient in the case of GDC and compared this value to literature as summarized in Table 1. On the other hand, thanks to the AFM mathematical toolbox, it was possible to estimate the GDC surface (5 X 5 μm^2) morphology changes before and after the beam irradiation at the conditions F=85mJ/cm^2 and V = 0.4 mm/s.

Conclusion

We demonstrate the feasibility of nanostructuring with quasi-periodic LIPSS on the complex oxide alloy formed by GDC/YSZ substrate using a UV picosecond laser beam with low repetition rate. Static and scanning irradiation modes were investigated according to the fluence and number of pulse. In the static mode, two unexpected LSFL orientations are formed within the same irradiated area for F varying from 85 up to 125 mJ/cm^2 but only for a low number of accumulated pulses (N<20). The parallel LSFL formation is supported by the thermochemical oxidation origin and the transition to the MIEC state that occurs in the center of the irradiated zone for higher accumulated energy dose. With higher number of pulses, the progressive ablation of the CDG film occurs to achieve a step by step removal of the film followed by the like-square patterning of the YSZ substrate. In the static mode and for equivalent conditions F = 85 mJ/cm^2 and $\boldsymbol{N_{eff} = 25}$, LSLF were formed on large scale area (4X4 mm2) with perpendicular orientation when more complex patterning was achieved at F=125 mJ/cm^2, and $\boldsymbol{N_{eff}}$ = 10 attributed to the overlap and the superposition of parallel and perpendicular LSFL. The scanning limits leading to the progressive ablation of the GDC film were also investigated until the full removal of the film and the starting point of YSZ substrate patterning. Finally the enhancement of the exchange surface area by a simple geometrical model and AFM direct measurements for the condition F = 85 mJ/cm^2 and V = 0,4 mm/s is estimated close to 33% and confirmed by direct AFM analysis.

References

[1] A. Nakhoul *et al.*, « Self-Organization Regimes Induced by Ultrafast Laser on Surfaces in the Tens of Nanometer Scales », *Nanomaterials*, vol. 11, nº 4, Art. nº 4, avr. 2021, DOI: 10.3390/nano11041020.

[2] L. P. Rivera, D. Munoz-Martin, A. Chávez-Chávez, M. Morales, G. Gómez-Rosas, et C. Molpeceres, « Subwavelength LIPSS formation on SS304 by picosecond laser irradiation under water confinement », *Mater. Sci. Eng. B*, vol. 273, p. 115393, nov. 2021, DOI: 10.1016/j.mseb.2021.115393.

[3] J. Bonse, H. Sturm, D. Schmidt, et W. Kautek, « Chemical, morphological and accumulation phenomena in ultrashort-pulse laser ablation of TiN in air »:, *Appl. Phys. Mater. Sci. Process.*, vol. 71, nº 6, Art. nº 6, déc. 2000, DOI: 10.1007/s003390000585.

[4] A. Borowiec et H. K. Haugen, « Subwavelength ripple formation on the surfaces of compound semiconductors irradiated with femtosecond laser pulses », *Appl. Phys. Lett.*, vol. 82, nº 25, Art. nº 25, juin 2003, DOI: 10.1063/1.1586457.

[5] A. De Zanet, V. Casalegno, et M. Salvo, « Laser surface texturing of ceramics and ceramic composite materials – A review », *Ceram. Int.*, vol. 47, nº 6, Art. nº 6, mars 2021, DOI: 10.1016/j.ceramint.2020.11.146.

[6] F. Costache, M. Henyk, et J. Reif, « Modification of dielectric surfaces with ultra-short laser pulses », *Appl. Surf. Sci.*, p. 6, 2002, DOI: 10.1016/S0169-4332(01)00675-4

[7] Q. Li *et al.*, « Femtosecond laser-induced periodic surface structures on lithium niobate crystal benefiting from sample heating », *Photonics Res.*, vol. 6, nº 8, Art. nº 8, août 2018, DOI: 10.1364/PRJ.6.000789.

[8] E. Stratakis *et al.*, « Laser engineering of biomimetic surfaces », *Mater. Sci. Eng. R Rep.*, vol. 141, p. 100562, juill. 2020, DOI: 10.1016/j.mser.2020.100562.

[9] J. Bonse, S. Hohm, S. V. Kirner, A. Rosenfeld, et J. Kruger, « Laser-Induced Periodic Surface Structures— A Scientific Evergreen », *IEEE J. Sel. Top. Quantum Electron.*, vol. 23, nº 3, Art. nº 3, mai 2017, DOI: 10.1109/JSTQE.2016.2614183.

[10] M. Ahn *et al.*, « Low damage electrical modification of 4H-SiC via ultrafast laser irradiation », *J. Appl. Phys.*, vol. 123, nº 14, p. 145106, avr. 2018, DOI: 10.1063/1.5020445.

[11] A. Y. Vorobyev et C. Guo, « Direct femtosecond laser surface nano/microstructuring and its applications: Direct femtosecond laser surface nano/microstructuring and its applications », *Laser Photonics Rev.*, vol. 7, nº 3, Art. nº 3, mai 2013, DOI: 10.1002/lpor.201200017.

[12] J. Reif, O. Varlamova, S. Uhlig, S. Varlamov, et M. Bestehorn, « On the physics of self-organized nanostructure formation upon femtosecond laser ablation », *Appl. Phys. A*, vol. 117, nº 1, Art. nº 1, oct. 2014, DOI: 10.1007/s00339-014-8339-x.

[13] E. L. Gurevich et S. V. Gurevich, « Laser Induced Periodic Surface Structures induced by surface plasmons coupled via roughness », *Appl. Surf. Sci.*, vol. 302, p. 118-123, mai 2014, DOI: 10.1016/j.apsusc.2013.10.141.

[14] P. Liu, W. Wang, A. Pan, Y. Xiang, et D. Wang, « Periodic surface structures on the surface of indium tin oxide film obtained using picosecond laser », *Opt. Laser Technol.*, vol. 106, p. 259-264, oct. 2018, DOI: 10.1016/j.optlastec.2018.04.019.
[15] C. Deng *et al.*, « Photocatalytic performance of TiO2 thin film decorated with Cu2O nanoparticles by laser ablation », *Opt. Mater.*, vol. 94, p. 130-137, août 2019, DOI: 10.1016/j.optmat.2019.05.030.
[16] T. T. D. Huynh, A. Petit, et N. Semmar, « Picosecond laser induced periodic surface structure on copper thin films », *Appl. Surf. Sci.*, vol. 302, p. 109-113, mai 2014, DOI: 10.1016/j.apsusc.2013.10.172.
[17] A. Talbi *et al.*, « Femtosecond laser irradiation of titanium oxide thin films: accumulation effect under IR beam », *Appl. Phys. A*, vol. 126, nº 5, Art. nº 5, mai 2020, DOI: 10.1007/s00339-020-03568-5.
[18] O. Varlamova, F. Costache, M. Ratzke, et J. Reif, « Control parameters in pattern formation upon femtosecond laser ablation », *Appl. Surf. Sci.*, vol. 253, nº 19, p. 7932-7936, juill. 2007, DOI: 10.1016/j.apsusc.2007.02.067.
[19] J. Bonse, A. Rosenfeld, et J. Krüger, « On the role of surface plasmon polaritons in the formation of laser-induced periodic surface structures upon irradiation of silicon by femtosecond-laser pulses », *J. Appl. Phys.*, vol. 106, nº 10, Art. nº 10, nov. 2009, DOI: 10.1063/1.3261734.
[20] J. Bonse et J. Krüger, « Pulse number dependence of laser-induced periodic surface structures for femtosecond laser irradiation of silicon », *J. Appl. Phys.*, vol. 108, nº 3, Art. nº 3, août 2010, DOI: 10.1063/1.3456501.
[21] S. K. Das, H. Messaoudi, A. Debroy, E. McGlynn, et R. Grunwald, « Multiphoton excitation of surface plasmon-polaritons and scaling of nanoripple formation in large bandgap materials », *Opt. Mater. Express*, vol. 3, nº 10, Art. nº 10, oct. 2013, DOI: 10.1364/OME.3.001705.
[22] A. Nechache et S. Hody, « Alternative and innovative solid oxide electrolysis cell materials: A short review », *Renew. Sustain. Energy Rev.*, vol. 149, p. 111322, oct. 2021, DOI: 10.1016/j.rser.2021.111322.
[23] Butz, Benjamin, « Yttria-Doped Zirconia as Solid Electrolyte for Fuel-Cell Applications », Laboratorium für Elektronenmikroskopie (LEM), 2009.
[24] B. Steele, « Appraisal of Ce1−yGdyO2−y/2 electrolytes for IT-SOFC operation at 500°C », *Solid State Ion.*, vol. 129, nº 1-4, Art. nº 1-4, avr. 2000, DOI: 10.1016/S0167-2738(99)00319-7.
[25] M. Mickan, P. Coddet, J. Vulliet, A. Caillard, T. Sauvage, et A.-L. Thomann, « Optimized magnetron sputtering process for the deposition of gadolinia doped ceria layers with controlled structural properties », *Surf. Coat. Technol.*, vol. 398, p. 126095, sept. 2020, DOI: 10.1016/j.surfcoat.2020.126095.
[26] J. Bonse, « Quo Vadis LIPSS?—Recent and Future Trends on Laser-Induced Periodic Surface Structures », *Nanomaterials*, vol. 10, nº 10, p. 1950, sept. 2020, DOI: 10.3390/nano10101950.
[27] J. Reif, F. Costache, M. Henyk, et S. V. Pandelov, « Ripples revisited: non-classical morphology at the bottom of femtosecond laser ablation craters in transparent dielectrics », *Appl. Surf. Sci.*, vol. 197-198, p. 891-895, sept. 2002, DOI: 10.1016/S0169-4332(02)00450-6.
[28] M. Mezera, J. Bonse, et G. R. B. E. Römer, « Influence of Bulk Temperature on Laser-Induced Periodic Surface Structures on Polycarbonate », *Polymers*, vol. 11, nº 12, p. 1947, nov. 2019, DOI: 10.3390/polym11121947.

[29] E. Rebollar, M. Castillejo, et T. A. Ezquerra, « Laser induced periodic surface structures on polymer films: From fundamentals to applications », *Eur. Polym. J.*, vol. 73, p. 162-174, déc. 2015, DOI: 10.1016/j.eurpolymj.2015.10.012.
[30] O. Shavdina, H. Rabat, M. Vayer, A. Petit, C. Sinturel, et N. Semmar, « Polystyrene Thin Films Nanostructuring by UV Femtosecond Laser Beam: From One Spot to Large Surface », *Nanomaterials*, vol. 11, n° 5, Art. n° 5, avr. 2021, DOI: 10.3390/nano11051060.
[31] A. V. Dostovalov *et al.*, « LIPSS on thin metallic films: New insights from multiplicity of laser-excited electromagnetic modes and efficiency of metal oxidation », *Appl. Surf. Sci.*, vol. 491, p. 650-658, oct. 2019, DOI: 10.1016/j.apsusc.2019.05.171.
[32] J. Bonse and S. Gräfm « Maxwell Meets Marangoni — A Review of Theories on Laser-Induced Periodic Surface Structures », Laser Photonics Rev. 2020, 14, 2000215, DOI: 10.1002/lpor.202000215.
[33] J. E. Sipe, J. F. Young, J. S. Preston, H. M. van Driel, « Laser-induced periodic surface structure. I. Theory », *Phys. Rev. B*, vol. 27, n° 2, Art. n° 2, janv. 1983, DOI: 10.1103/PhysRevB.27.1141.
[34] A. V. Dostovalov, V. P. Korolkov, K. A. Okotrub, K. A. Bronnikov, et S. A. Babin, « Oxide composition and period variation of thermochemical LIPSS on chromium films with different thickness », *Opt. Express*, vol. 26, n° 6, p. 7712, mars 2018, DOI: 10.1364/OE.26.007712.
[35] B. Öktem *et al.*, « Nonlinear laser lithography for indefinitely large-area nanostructuring with femtosecond pulses », *Nat. Photonics*, vol. 7, n° 11, p. 897-901, nov. 2013, DOI: 10.1038/nphoton.2013.272.
[36] S. R. Bishop, K. L. Duncan, E. D. Wachsman, « Thermo-Chemical Expansion in Strontium-Doped Lanthanum Cobalt Iron Oxide: Thermo-Chemical Expansion in LSCF », *J. Am. Ceram. Soc.*, vol. 93, n° 12, p. 4115-4121, déc. 2010, DOI: 10.1111/j.1551-2916.2010.03991.x.
[37] Y. Kuru, M. Usman, G. Cristiani, et H.-U. Habermeier, « Microstructural changes in epitaxial YBa2Cu3O7−δ thin films due to creation of O vacancies », *J. Cryst. Growth*, vol. 312, n° 20, p. 2904-2908, oct. 2010, DOI: 10.1016/j.jcrysgro.2010.06.030.
[38] S. R. Bishop, H. L. Tuller, Y. Kuru, et B. Yildiz, « Chemical expansion of nonstoichiometric Pr0.1Ce0.9O2−δ: Correlation with defect equilibrium model », *J. Eur. Ceram. Soc.*, vol. 31, n° 13, p. 2351-2356, nov. 2011, DOI: 10.1016/j.jeurceramsoc.2011.05.034.
[39] Y.-F. Gao *et al.*, « Picosecond laser-induced periodic surface structures (LIPSS) on crystalline silicon », *Surf. Interfaces*, vol. 19, p. 100538, juin 2020, DOI: 10.1016/j.surfin.2020.100538.
[40] J. Bonse, J. Krüger, S. Höhm, et A. Rosenfeld, « Femtosecond laser-induced periodic surface structures », *J. Laser Appl.*, vol. 24, n° 4, Art. n° 4, sept. 2012, DOI: 10.2351/1.4712658.
[41] A. Talbi, C. T. Tameko, A. Stolz, E. Millon, C. Boulmer-Leborgne, et N. Semmar, « Nanostructuring of titanium oxide thin film by UV femtosecond laser beam: From one spot to large surfaces », *Appl. Surf. Sci.*, vol. 418, p. 425-429, oct. 2017, DOI: 10.1016/j.apsusc.2017.02.033.
[42] M. Ehrhardt, B. Han, F. Frost, P. Lorenz, et K. Zimmer, « Generation of laser-induced periodic surface structures (LIPSS) in fused silica by single NIR nanosecond laser pulse irradiation in confinement », *Appl. Surf. Sci.*, vol. 470, p. 56-62, mars 2019, DOI: 10.1016/j.apsusc.2018.11.119.

[43] L. Parellada-Monreal, I. Castro-Hurtado, M. Martínez-Calderón, L. Presmanes, et G. G. Mandayo, « Laser-induced periodic surface structures on ZnO thin film for high response NO2 detection », *Appl. Surf. Sci.*, vol. 476, p. 569-575, mai 2019, DOI: 10.1016/j.apsusc.2019.01.115.

List of Captions

Figure 1: Schematic of experimental setup process for GDC laser texturing, and (bellow) the corresponding S-scanning mode.

Figure 2: SEM image on the irradiated CDG film, for F = 125 mJ/cm^2 and N = 10 pulses. The insets show the non-irradiated (untreated) surface as well as two different LIPSS patterns (LSFL$_{//}$ and LSFL$_{\perp}$) and the transition zone. W_0 is the beam spot size; $W_{\perp}$ and $W_{//}$ are the estimated diameters of LSFL$_{\perp}$ and LSFL$_{//}$ regions, respectively.

Figure 3: Spatial period of parallel (Λ LSFL$_{//}$) and perpendicular (Λ LSFL$_{\perp}$) LIPSS function of the laser fluence F under static irradiation case with 10 pulses.

Figure 4: SEM images of the GDC/YSZ films irradiated in static mode for different fluence values and number of pulses (a to i). Horizontally, the laser fluence is fixed and the number of laser pulses is increased from 10 to 40 then 50 or 70. Vertically, the laser fluence is increased from 40 to 105 then 125 mJ/cm^2. For (d) and (g), the upper (lower) images were taken at the border (center) of the laser spot.

Figure 5: EDX signals of the (a) untreated GDC film and films irradiated under different static laser conditions (b, c and d). SEM images of the corresponding film surfaces are also shown in the inset of each EDX spectrum.

Figure 6: Mapping of the laser induced surface modification of GDC on YSZ depending on laser fluence (y-axis) and number of laser pulses (x-axis).

Figure 7: Schematic view of the dependence of the LSFL formation typology for three regimes applied on the GDC surface. W_{YSZ} is the threshold diameter that corresponds to the full GDC ablation/YSZ structuring. The progressive ablation of GDC/YSZ film is shown on the diagram versus the energy dose.

Figure 8: SEM images showing the comparison of two irradiation conditions in scanning mode related to the static mode by the effective number of pulse $\boldsymbol{N_{eff}}$.

Figure 9: SEM images showing the evolution of the surface of the GDC/YSZ films irradiated in scanning mode for different laser fluences and scanning speeds (a1 to d2). Horizontally, the laser fluence is fixed and the scanning speed is varied from 0.4 to 0.2 mm/s. Vertically, the scanning speed is fixed and the laser fluence is increase from 85 to 150 mJ/cm^2. Laser polarization is shown as the two-headed white arrow.

Figure 10: SEM images of the transverse section of GDC: (a) Untreated surface and (b) After irradiation in scanning mode at F = 85 mJ/cm^2 and V = 0.4 mm/s.

Figure 11: RBS spectroscopy for untreated and textured GDC/YSZ film at a F = 85 mJ/cm^2 and V = 0.4 mm/s.

Figure 12: SEM and 3D AFM images of the cross section of GDC/YSZ film for F = 85 mJ/cm^2, V = 0.4 mm/s.

List of figures

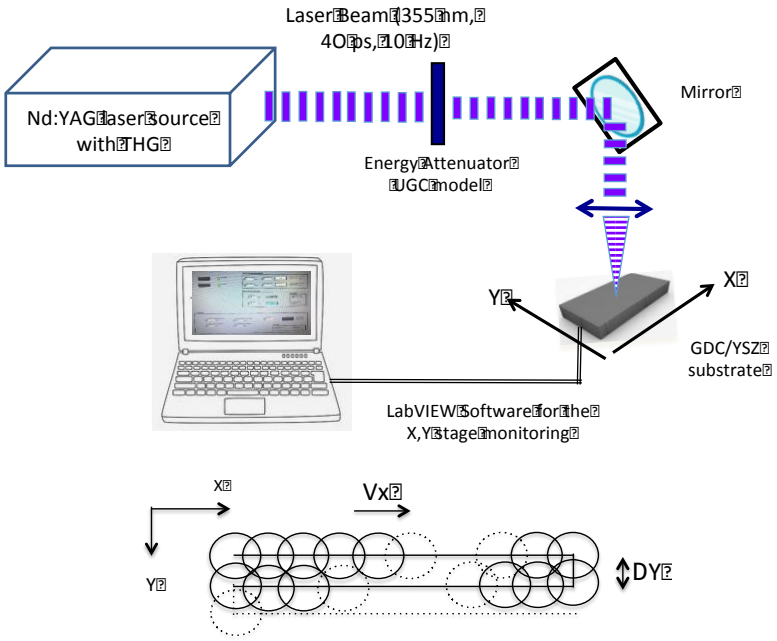

Figure 1

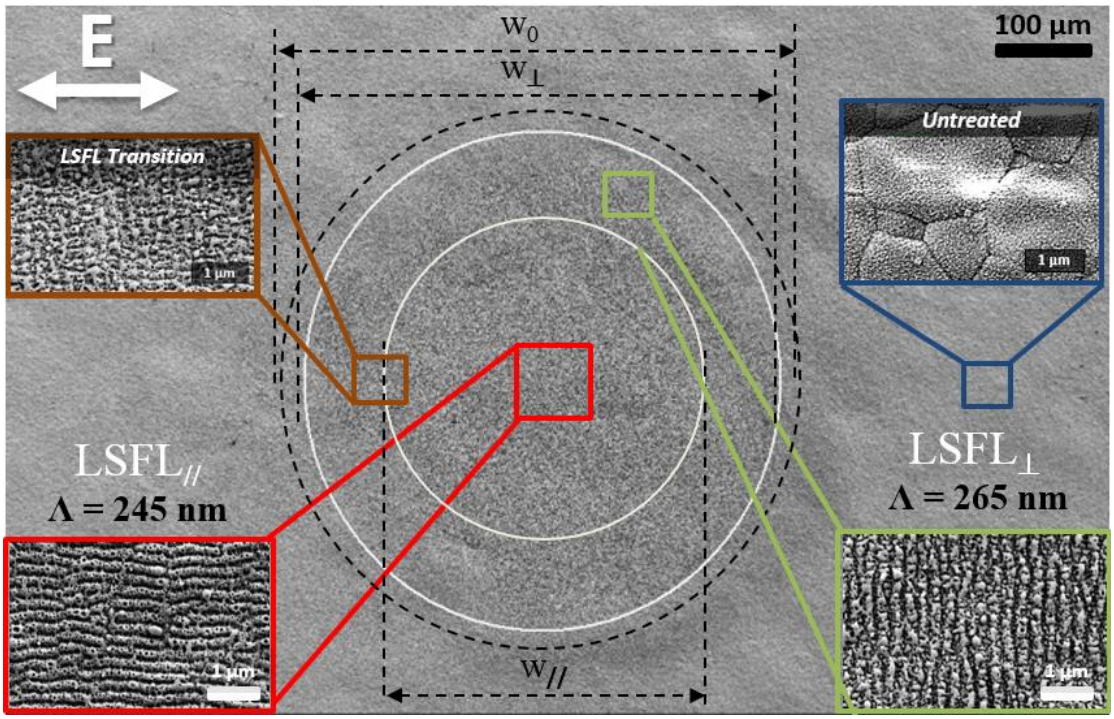

Figure 2

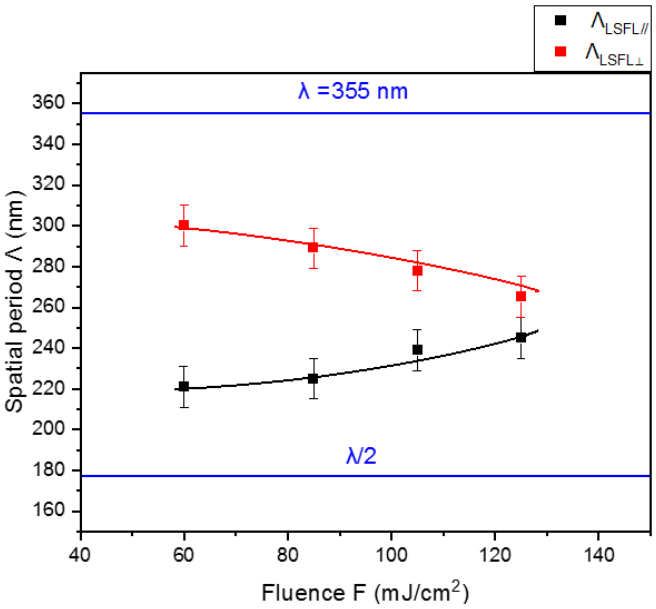

Figure 3

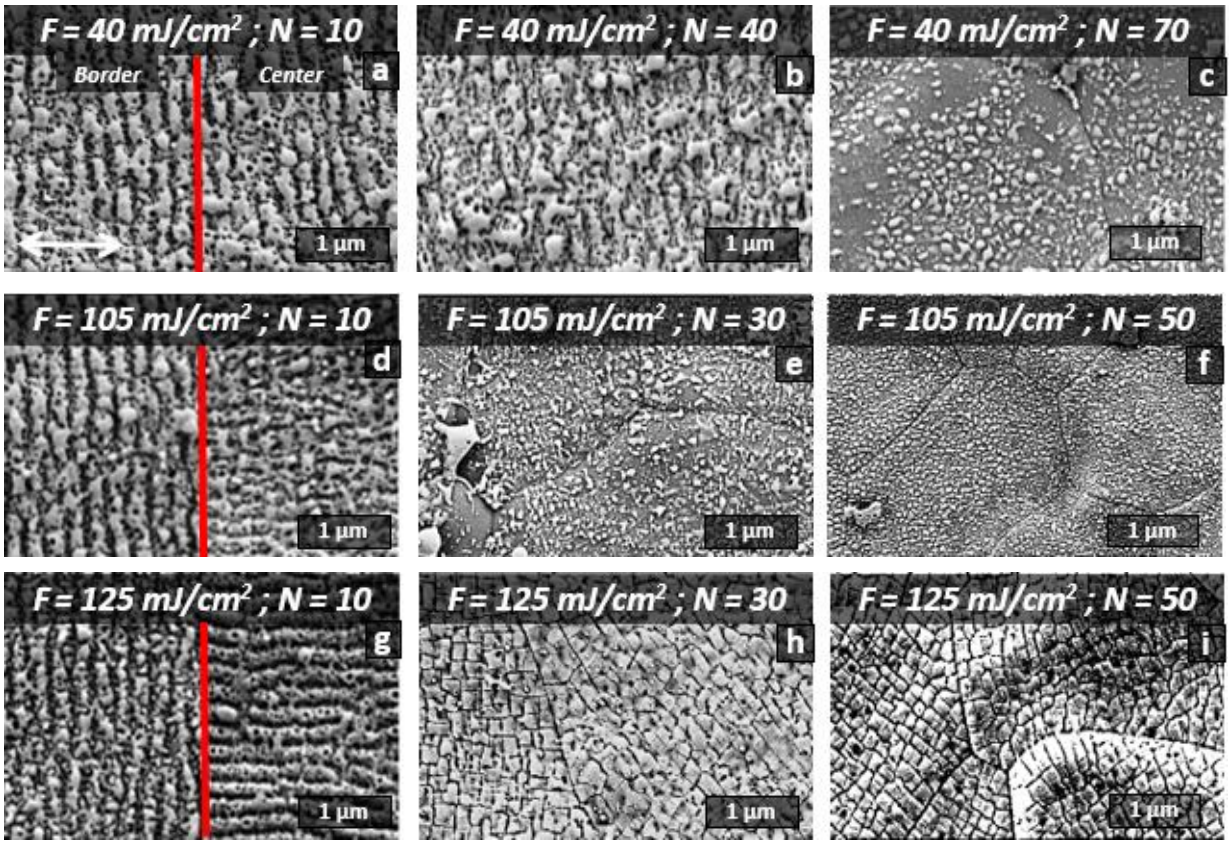

Figure 4

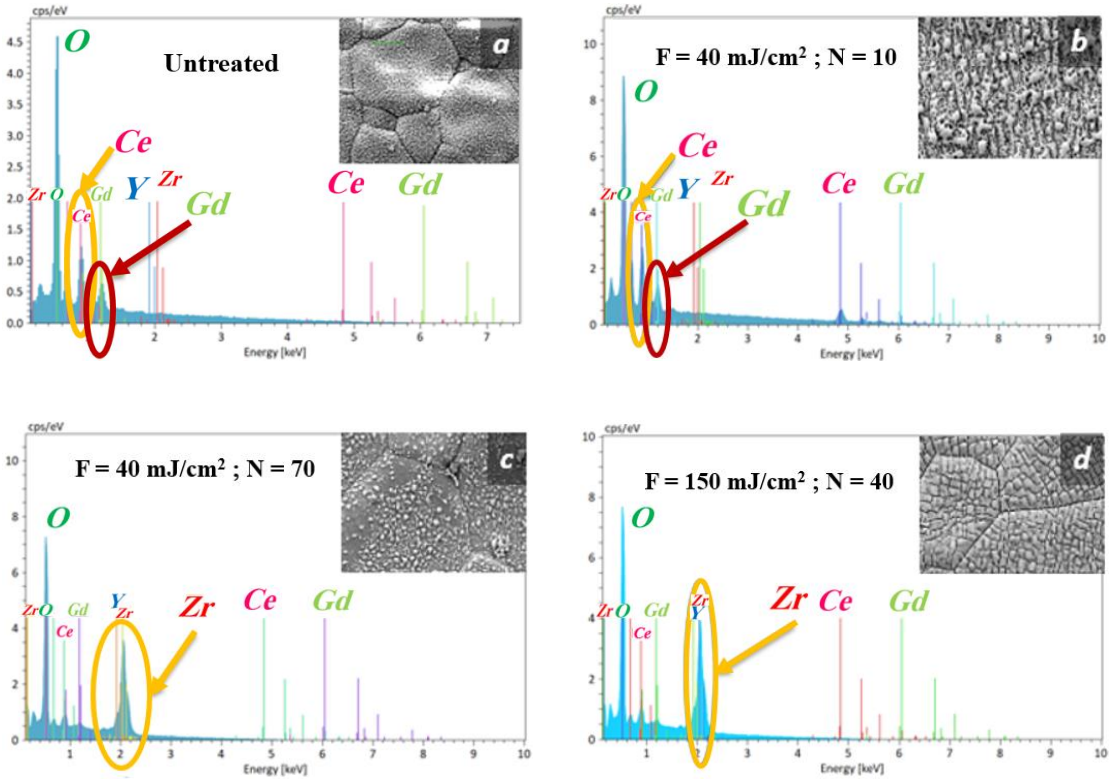
cps/eV
Untreated
a
O
Ce
Y
Zr
Gd
Energy [keV]
F = 40 mJ/cm² ; N = 10
b
F = 40 mJ/cm² ; N = 70
c
F = 150 mJ/cm² ; N = 40
d

Figure 5

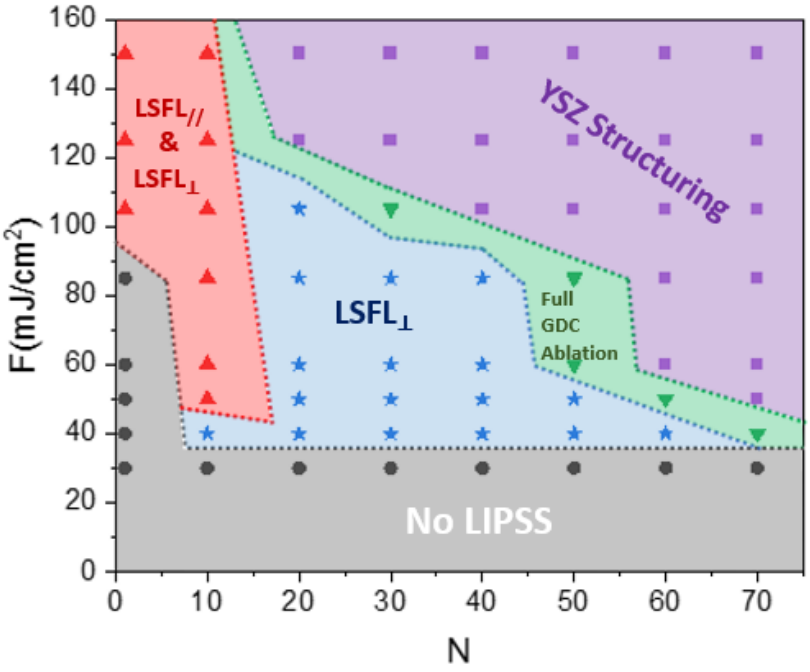

Figure 6

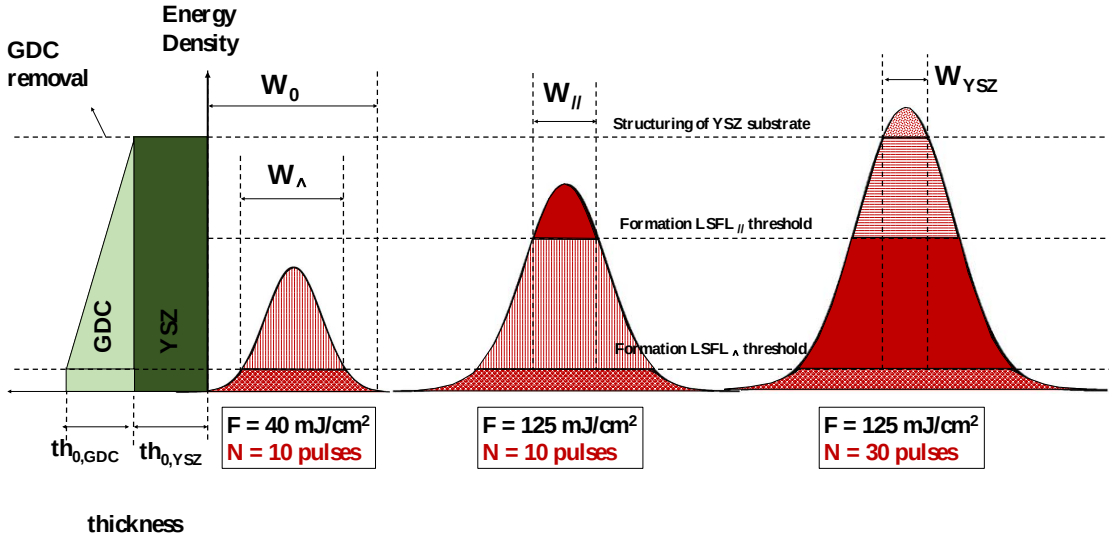

Figure 7

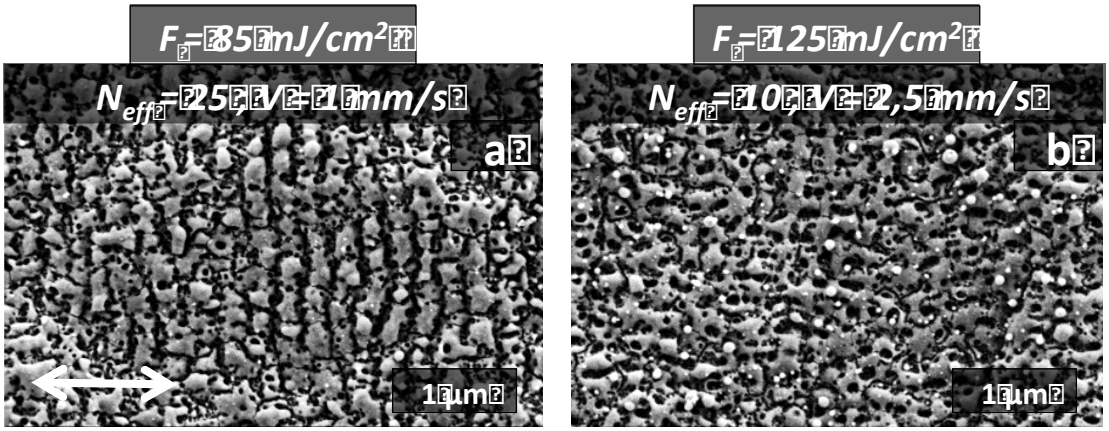

Figure 8

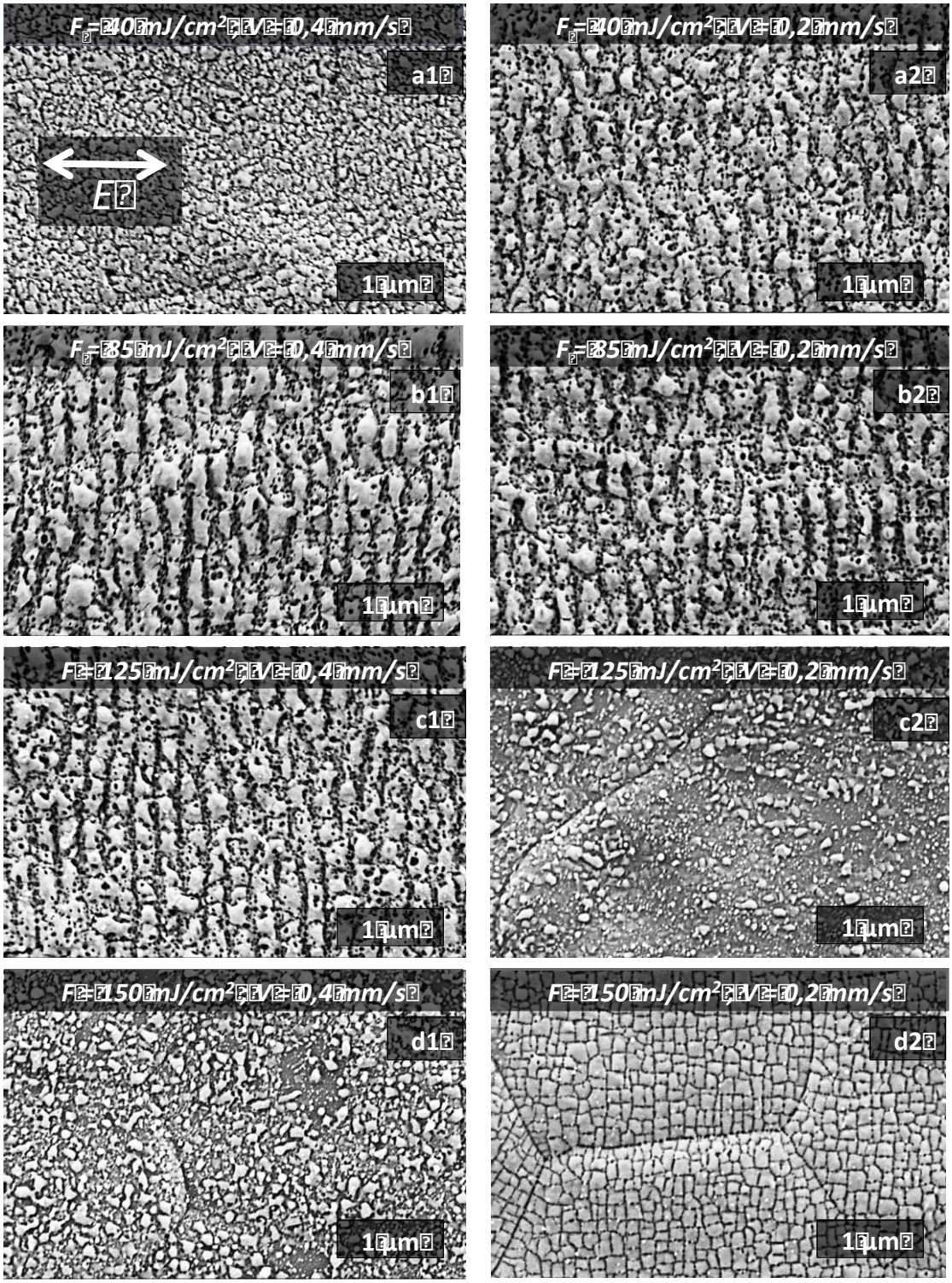
F=40 mJ/cm², V=0,4 mm/s
a1
E
1 µm
F=40 mJ/cm², V=0,2 mm/s
a2
1 µm
F=85 mJ/cm², V=0,4 mm/s
b1
1 µm
F=85 mJ/cm², V=0,2 mm/s
b2
1 µm
F=125 mJ/cm², V=0,4 mm/s
c1
1 µm
F=125 mJ/cm², V=0,2 mm/s
c2
1 µm
F=150 mJ/cm², V=0,4 mm/s
d1
1 µm
F=150 mJ/cm², V=0,2 mm/s
d2
1 µm

Figure 9

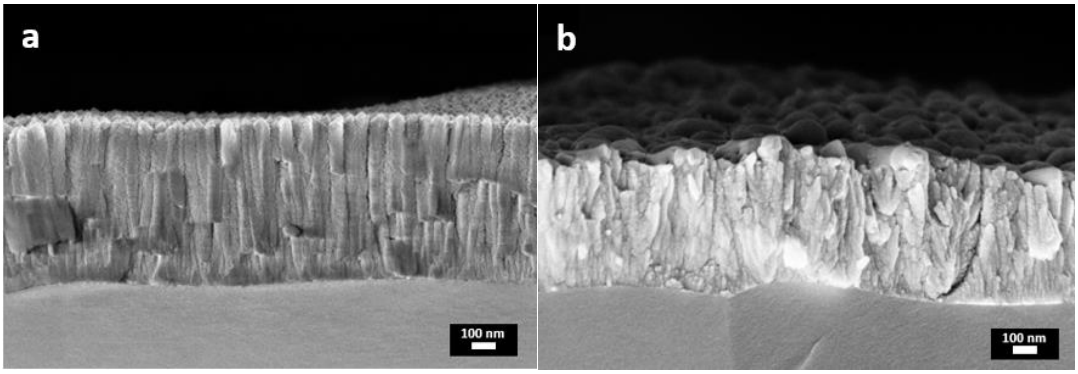

Figure 10

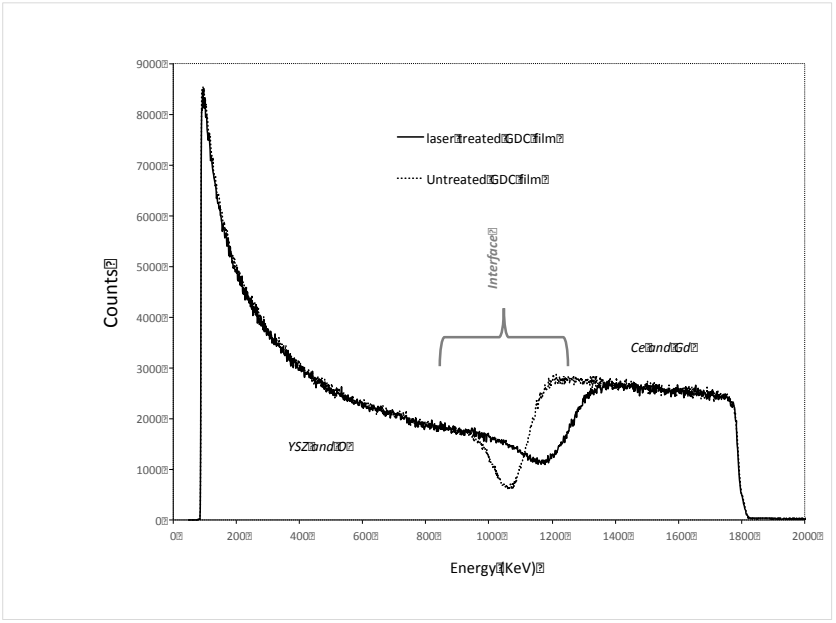

Figure 11

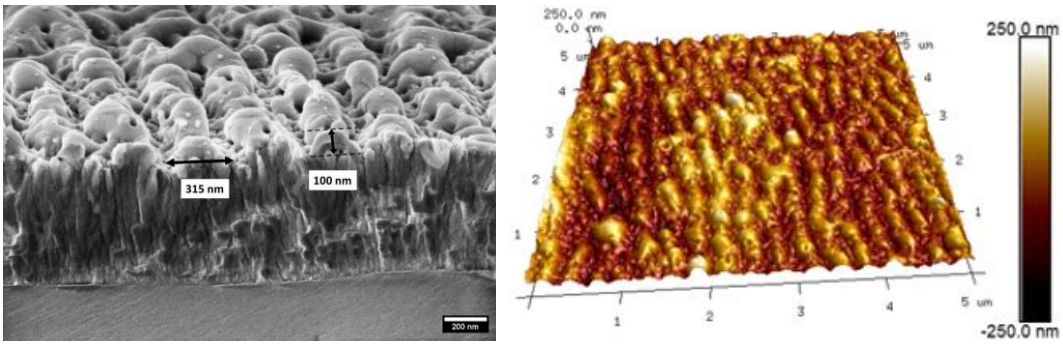

Figure 12

List of Tables

Refs	laser / wavelength (nm)	Materials/ nanostructures	Period λ1 (nm)	Period λ2 (nm)	Specific size R_{eq} (nm)	Σ (%)
D.D. Huynh [16]	Nd:YAG (40 ps)	Cu	270	200	68	127
	266	*Nano-dots 2D*				
Nakhoul [1]	Ti: Sapphire (25 fs)	Ni	110	--	32	134
	800	*Nano-bumps 1D*				
A. Talbi [17]	Yb:YKW (500 fs)	$TiO_{1.8}$	800	--	142	120
	1030	*LSFL 1D*				
Gao [39]	picosecond laser (8 ps)	Si	528	--	104	122
	532	*LSFL 1D*				
J. Bonse [40]	Ti: Sapphire (150 fs)	Ti	590	--	171	133
	800	*LSFL 1D*				
A. Talbi [41]	Ti: Sapphire (100 fs)	TiO_X	400	200	50	110
	266	*Nano-Spikes 2D*				
Ehrhardt [42]	fibre laser (25 ns)	SiO_2	500	--	163	137
	1064	*LSFL 1D*				
Parellada-Monreal [43]	Ti: Sapphire (130 fs)	ZnO	145	--	50	140
	800	*HSFL 1D*				
Dostavalov [31]	PHAROS 6W laser (232 fs)	Cr	696	--	155	125
	1064	*LSFL //, LSFL⊥*				
This Work	**Nd:YAG (40 ps)**	**GDC**	**260**	--	**76**	**133**
	355	***LSFL //***				

Table 1: Surface enhancement coefficient (**Σ**) versus LIPSS size and periods.

APPENDIX

Estimation of the surface enhancement by LIPSS

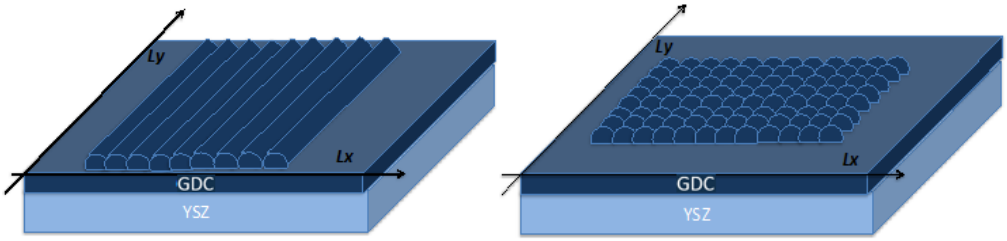

(a- 1D) **(b- 2D)**

Figure A-1: Schematic of 1D and 2D LIPSS structures respectively plotted by hemiscylinders (a) and hemispheres (b).

As illustrated on fig A-1, we consider as a starting point a thin film surface (GDC in the present case) with a thickness (e), and a flat rectangular surface (S_0) given by:

$$S_0 = Lx.\times Ly \quad (1)$$

Assuming that contiguous regular ripples are approximated by hemicylinders (HCL) shape, and contiguous dots or bumps by hemispheres (HSP) with uniform radius (r, with $2r \leq Lx, Lx$. The number of nano-structures *Nx* and *Ny* in the x and y directions are respectively given by:

$$Nx = \frac{Lx}{2r};\ \ Ny = \frac{Ly}{2r} \quad (2)$$

Considering the specific surfaces of each HCL and HSP, respectively S_{HCL} and S_{HSP}, with $S_{HCL} = (2\pi r \times Ly/2)$; and $S_{HSP} = (4\pi r\text{^}2/2)$, the 'resonant' corresponding surfaces are easily deduced thanks to the following equations:

$$S_{tHCL} = Nx \times S_{HCL} \quad (3)$$

$$S_{tHSP} = Nx \times Ny \times S_{HSP} \quad (4)$$

S_{tHCL}, S_{tHSP} are corresponding to the total resonant surface in case 1D or 2D 'isotropic' nanostructures. The ratio of the surface enhancement (Σ) due to the LIPSS formation could be then easily deduced thanks to the set of expressions (1) to (3).

In the case of 1D contiguous nanostructures (regular ripples) the ratio (Σ_{HCL}) is calculated by dividing (3) on (1), and thus:

$$\Sigma_{HCL} = \frac{S_{tHCL}}{S_0} = \frac{\pi}{2} \quad (5)$$

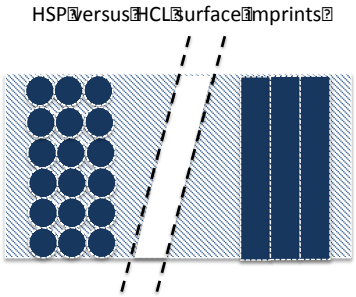

Figure A-2: Top view of nano-hemispheres (HSP) and nano-hemicylinders (HCL) imprints.

In this particular case, the HCL imprints on the surface are basically similar to S_0 (See fig. A-2) and thus equation (5) becomes sufficient to calculate Σ_{HCL}. This is not the case with the HSP imprints and the resonant surface should be calculated according to the following equation:

$$\Sigma_{HSP} = \frac{(S_0 - S_{nr}) + S_{tHSP}}{S_0} = 1 + \frac{S_{tHSP} - S_{nr}}{S_0} = 1 + \frac{\pi}{4} \quad (6)$$

The main result from (5) and (6) is that the surface enhancement is basically controlled by the shape of nanostructures (nano-spheres, nanocylinders…), and in the particular case these contiguous structures, the maximum surface increase could not exceed ***57% with HCL*** and ***78,5% with HSP***.

However LIPSS are often exhibiting more complex shapes and patterns (nanodots, nanopillars, spikes, grooves…) with space conformation that corresponds to LSFL or HSFL, meaning strongly correlated to the laser beam wavelength. In this case, the previous set of equations should add the LIPSS period as a key-parameter for the estimation of the surface enhancement coefficient (Σ^*).

Generalized equations for surface enhancement by LIPSS

Considering the configuration of thin films with nanodots, for example the case reported in reference [41] and shown in fig. A-3, LSFL as well HSFL are controlled by their spatial period λ1 and λ2 respectively in the X and Y directions.

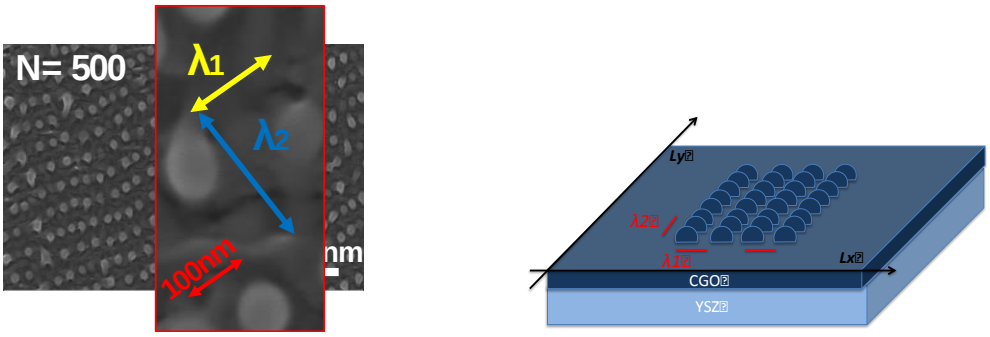

(a) **(b)**

Figure A-3: 2D nanostructures: (a) TiOx nanodots from A. Talbi et al.[41], (b) schematic view of the (a) situation.

In this case, the number N^*x and N^*y are deduced from equation (2), by replacing 2r by *λ1 in the X direction*, and 2r by *λ2* in the Y one. That means:

$$N^*x = \frac{Lx}{\lambda 1},\ and \quad N^*y = \frac{Ly}{\lambda 2} \qquad (2^*)$$

By applying the same calculation steps, from equation (2) to (4), the expression of the surface enhancement coefficient (Σ^*) becomes then:

$$\Sigma HCL^* = 1 + \frac{S_{tHCL} - S_{nr}}{S_0} = 1 + \left(\frac{2r}{\lambda 1}\right)\left[\frac{\pi}{2} - 1\right] \qquad (5^*)$$

$$\Sigma HSP^* = 1 + \frac{S_{tHSP} - S_{nr}}{S_0} = 1 + \frac{\pi}{4}\left(\frac{2r}{\lambda 1}\right)\left(\frac{2r}{\lambda 2}\right) \qquad (6^*)$$

It is easy to check that when both λ1 and λ2 are equal to 2r (previous case of contiguous HSP), we find again the same results that in equations (3) and (4). The correlation of the Σ^* coefficient to the ratio (2r/λ) becomes explicit in equations (4*) and (5*) and can be extended to other surface morphologies (cones, cylinders…) by replacing the specific surface of each nano-object by their equivalent hemi-spherical surface, and thus their specific radius r.